Geophysical Fluid Dynamics, 1973, Vol. 4, pp. 297–332

Printed in Great Britain

Baroclinic Instability in Ocean Currents

ISIDORO ORLANSKI and MICHAEL D. COX

Geophysical Fluid Dynamics Laboratory/NOAA Princeton University, Post Office Box 308 Princeton, New Jersey 08540, U.S.A.

(*Received April 24, 1972*)

Unstable waves in a western boundary current are investigated in a full three-dimensional, numerical model. A numerical integration is carried out which traces the evolution of a growing wave on an initially uniform current with vertical shear. As indicated in earlier analytic studies based on simpler 2-layer models (Orlanski, 1969) the current is baroclinically unstable for the observed parameter range of the Gulf Stream.

Large meanders of the jet in the western boundary current are noticeable within 10 days. Finite amplitude effects, which can be investigated by the numerical model, reduce the growth rate of the disturbance by nearly an order of magnitude compared to linear theory. Comparison with observations indicate that the meanders of the Florida Current between Miami and Hatteras are probably baroclinically unstable waves.

Introduction

It has been recognized for some time that the dynamics of the ocean and atmosphere are closely analgous. Similar phenomena take place from the high frequency range characterized by internal gravity waves to the low range of frequencies dominated by quasi-geostrophic motion. Detailed temperature measurements indicate that the ocean has relatively large-scale density discontinuities that are very much like atmospheric fronts. The oceanic fronts have a characteristic slope which is determined by the density difference, rotation and vertical shear of the currents parallel to the front. Meandering currents are observed in those parts of the ocean where strong density gradients are strongest, such as the Gulf Stream and Kuroshio regions. Since atmospheric fronts are known to be baroclinically unstable, it appears to be appropriate to suspect the same mechanism may be present in the ocean. This point has been investigated in an earlier analytic study by the author of the stability on a two-layer model. Before going into the details

of this study, we shall try to describe in a very simple way how a baroclinically unstable wave can develop when horizontal density gradients are present.

The argument is not a new one (Charney (1947), Smagorinsky (1963), Pedlosky (1964), etc.). It has been used to describe the instability mechanism for large scale quasi-geostrophic atmospheric waves. Here, we shall point out that we do not restrict ourselves to waves that have very low frequencies (quasi-geostrophic waves). In fact, they can even have frequencies close to the inertial frequency; but we shall return to this point later.

Assume that we have a cross section of the density field as shown in Figure 1(a) where the constant density lines have an angle α with the horizontal. Since any type of motion with any type of slope is possible, we will look at four different trajectories to see when the system can be unstable.

Suppose we force a particle to move in a plane, A to A'. Since the particle is heavier at A than when it is displaced to A' where the environment is lighter, it will feel a restoring force proportional to the difference in density. Consequently, the particle will return to its original position, and if the fluid is inviscid, it will overshoot the original position and oscillate. This type of motion can be called an internal gravity wave.

If the particle is displaced in the plane, B to B' where the particle density at B is heavier than at B', but the gravity force due to this difference acts perpendicular to the plane, the particle will feel no restoring force and will remain in its new position.

Now, if we consider the plane C to C', again the particle is heavier at C than at C'. However, in this case the gravity force will act to accelerate the particle past C' and conversely, a particle in C' that moves to C will feel the gravity force lifting the particle. Therefore, motion in these planes will be amplified. It is possible to see that in this case the velocity is continuously increasing as well as the kinetic energy, but since lighter fluid moves to regions of heavier fluid and vice-versa in average, the horizontal density gradient will diminish. Accordingly, the available potential energy will decrease and a clear conversion from potential energy to kinetic energy can be deduced by these unstable processes (Baroclinic Instability).

Finally, since the particles in the last plane, D to D', have the same density, they will not feel any restoring force and the plane will be neutral.

We can deduce then from this simple argument that any motion between B and D or with trajectory planes where the angle will be less than α, the system must be unstable regardless of the frequency or the horizontal scale that the motion has. The only restrictions for frequencies or scales are that the time variation of the mean density pattern, which we have described, is larger than the wave period and also that the uniformity in the horizontal scale must be larger than the wavelength of the unstable waves. On the basis

of these restrictions, the most unstable slope for the waves will be given by:

$$\frac{w}{u} \approx -\frac{1}{2} \propto$$

where w and u are the vertical and horizontal velocity respectively and $\propto$ is the slope of constant density and can be written:

$$\propto = \rho_x/\rho_z$$

Charney (1947) and Pedlosky (1964) demonstrate that either the variation in the Coriolis parameter (β) or a slope in the topography in the lower boundary will reduce the angle $\propto$ where the waves can be unstable. They conclude that if these elements are included, the system will be more stable.

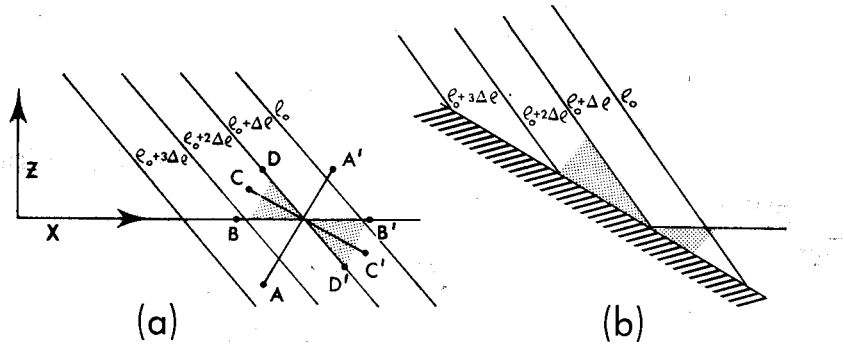

FIGURE 1(a) Different trajectories that could be unstable (shaded area) in a baroclinic fluid. (b) The bottom slope in relation to slope of the maximum instability.

Orlanski (1969) previously discussed this type of instability for the Gulf Stream showing that, in the opposite sense, the bottom topography can destabilize the system. Furthermore, from the argument we are following, if we assume that the ground has a certain slope, as in Figure 1b, it will seem natural to say that any type of horizontal motion will induce a vertical motion proportional to the bottom slope by the continuity equation:

$$w = \mathbb{V}_H \nabla h \approx u h_x \,.$$

Then, if h_x is equal to $1/2\ \rho_x/\rho_z$, which is the slope of maximum instability, the slope of the bottom topography will induce the waves to always have a plane that corresponds to the maximum unstable waves. This last criterion will only be true if the strong horizontal density gradients are close to the

bottom topography. For example, consider the coastal boundary currents in the ocean.

Using an argument similar to the one previously discussed, we can predict the scale of the baroclinically unstable waves. Let us assume that the mean state is in geostrophic balance, then the horizontal density gradient will be related to the vertical shear flow as follows:

$$\rho_x = \frac{-fV_z}{g}.$$

Substituting in the expression for the slope of the isopycnics:

$$\propto = \frac{-fV_z}{N^2},$$

where $[N^2 = (-g\rho_z/\rho_o)]$ is the square of the Brunt-Vaisala frequency. Now, if the Rossby number is defined as $[R_o = (V/f\lambda)]$, where λ is the scale of horizontal length in which V varies, $\propto$ can be expressed by:

$$\propto = \frac{-f^2}{N^2} R_o \frac{\lambda}{H}, \quad \text{where}$$

H is the height of the vertical variation of V, or the depth of the fluid. Then the slope of the maximum unstable waves is:

$$\frac{w}{u} = \frac{1}{2}\frac{f^2}{N^2} R_o \frac{\lambda}{H}.$$

We must distinguish two different cases to evaluate the ratio of (w/u) from the continuity equation. If we are looking in a regime of small R_o, it can be shown from potential vorticity arguments that the magnitude of w will be:

$$w \approx R_o \frac{H}{l} u,$$

where l is the horizontal wavelength. Using the previous relation, the magnitude of the horizontal wavelength will be given by:

$$l \approx \frac{2}{\lambda}\left(\frac{H^2N^2}{f^2}\right) \approx \frac{2a^2}{\lambda},$$

where a is the Rossby radius of deformation for a stratified flow. We can see then that for atmospheric waves where $a = 1000$ km ($H = 10^4$ m, $N = 10^{-2}S^{-1}$) as well as $\lambda = 1000$ km, the wavelength for cyclone waves, is on the order of 2000 km. For the Gulf Stream over the continental shelf, with $a = 70$ km ($H = 10^3$ m, $N \sim 7 \times 10^{-3}S^{-1}$) and $\lambda = 100$ km, the wavelength will be on the order of 100 km. On the other hand, for a region of the

Gulf Stream in the deep ocean where $a = 120$ km ($H = 4 \times 10^3$ m, $N \approx 3 \times 10^{-3} S^{-1}$) and again $\lambda = 100$ km, the wavelength will be about 300 km. A similar estimation can be made for the Antarctic circumpolar current; there the wavelength will be on the order of 1000 km.

Notice that we previously assumed R_o to be small in finding the scale of l; however, this is not necessary because if R_o is on the order of unity, [$w = (H/l)u$], then l will be given by:

$$l = \frac{2a^2}{R_o \lambda}.$$

However, since R_o is the order of unity, the expression of l will be the same as used before.

In order to present a representative model of this type of wave in the ocean, we will use a three-dimensional model with continuous stratification and similar characteristics as those in the area of the Gulf Stream over the continental shelf. The dynamics in this region has been discussed by many scientists and a complete reference can be seen in Orlanski (1969). In each discussion linear theories were used to describe the unstable waves. In this paper, we will present the integration of a completely non-linear system.

1. Description of the model

The numerical model used in this study is basically that described in Bryan (1969) with only minor variations. The equations of motion are the Navier-Stokes equations with three basic modifications. The Boussinesq approximation is made in which variations of density are neglected except in the buoyancy term. Hydrostatic balance is assumed.

Viscosity and conductivity are replaced by new terms representing the diffusion of momentum and heat by small scale transient disturbances. A β-plane coordinate system is used in which both the vertical component of rotation and its latitudinal derivative appear in the equations as constants.

Let

$$n_o = \sin 35^\circ$$

$$u = \dot{x}$$

$$v = \dot{y} \tag{1.1}$$

The equations of motion are:

$$u_t + \mathscr{T} u - 2\Omega n_o v = -(\rho/\rho_o)_x + F^x \tag{1.2}$$

$$v_t + \mathscr{T} v + 2\Omega n_o u = -(\rho/\rho_o)_y + F^y \tag{1.3}$$

where the advection operator is defined by:

$$\mathcal{T}\mu = (u\mu)_x + (v\mu)_y + (w\mu)_z \tag{1.4}$$

and the effects of turbulent diffusion and viscosity are:

$$F^x = A_v u_{zz} + A_h(u_{xx} + u_{yy}) \tag{1.5}$$

$$F^y = A_v v_{zz} + A_h(v_{xx} + v_{yy}) \tag{1.6}$$

where A_v and A_h are coefficients of vertical and horizontal diffusion respectively. The continuity equation is:

$$w_y + u_x + v_y = 0 \tag{1.7}$$

and the hydrostatic relation is:

$$\rho g = -P_z \tag{1.8}$$

If a linear equation of state is assumed, then salinity may be eliminated from the model by the use of an apparent temperature T (Bryan and Cox 1967) such that:

$$\rho = \rho_o(1 - \alpha T) \tag{1.9}$$

where α is the thermal expansion coefficient. The conservation equation is:

$$T_t + \mathcal{T}T = \frac{A_y}{\delta} T_{zz} + A_h(T_{xx} + T_{yy}) \tag{1.10}$$

where δ is defined by:

$$\delta = \begin{cases} 1 & (\rho)_z < 0 \\ 0 & (\rho)_z > 0 \end{cases} \tag{1.11}$$

The boundary conditions at lateral walls are: Non-slip condition for velocity field and the adiabatic condition

$$u, v = 0 \text{ and } \frac{\partial T}{\partial X_m} = 0 \tag{1.12}$$

for the temperature field.

Where X_m is the coordinate normal to the wall. It seems justified to use those conditions over the left wall but on the right hand side it is rather artificial since the channel does not cover the entire ocean. However, we assume that most of the disturbance will be generated in the left of the channel (the place in which the baroclinicity is maximum) and will decay exponentially to the right wall. At upper and lower boundaries,

$$\frac{\partial u}{\partial z}, \frac{\partial v}{\partial z}, \frac{\partial T}{\partial z} = 0 \tag{1.13}$$

The vertical velocity is taken to be zero at the surface ("rigid lid" approximation) permitting a more efficient calculation. This restriction filters out high speed surface gravitational-inertial waves which would otherwise limit the length of the timestep of integration. At the bottom,

$$w = uH_x + vH_y \tag{1.14}$$

where H is depth.

Having specified a rigid lid, it is possible to define a transport stream function such that:

$$\psi_x = \int_{-H}^{0} \rho_o v dz$$

$$\psi_y = -\int_{-H}^{0} \rho_o u dz \tag{1.15}$$

and

The velocities are then calculated in two parts:

$$u = \bar{u} + \hat{u}$$

and

$$v = \bar{v} + \hat{v}$$

where $\bar{u}$, $\bar{v}$ represent the vertically averaged motion and $\hat{u}$, $\hat{v}$ are the deviations from the vertically averaged motion. The deviations $\hat{u}$, $\hat{v}$ are calculated from a vertically differentiated form of equations (1.2 and 1.3). The vertical differentiation permits the elimination of pressure from the equations by use of Eq. (1.8). The questions are then integrated vertically to obtain a solution for ψ, which in turn yields the vertically averaged motion $\bar{u}$, $\bar{v}$. The equations are transformed to finite difference form and integrated over time from an arbitrary initial state. The differencing scheme is the same as that of Bryan (1969).

2. Initial conditions

In order to achieve an idealization of the steady state condition of the Gulf Stream, in the area of Miami to Cape Hatteras, it is assumed that the North-South velocity is in geostrophic balance with the temperature field. This assumption is used as an initial condition for the model. Accordingly, a suitable analytic expression of the temperature can be defined as follows:

$$T_{(x)} = T_o - \Delta T(3 - 2(\delta x + 1)e^{-\delta x})(z\varepsilon - 1)e^{2\varepsilon z} \tag{2.1}$$

in which the parameters δ, ε, T_o, and ΔT can be fixed in such a way that they will meet the realistic conditions. The horizontal gradient of temperature at

the surface is about 12°/500 km and by using Eq. 2.1, we find that the surface temperature is given by:

$$T_{(x,o)} = T_o + \Delta T[3 - (2\delta x + 1)e^{-\delta x}] \tag{2.2}$$

where T_o will be fixed by the deep water temperature (4°C) and δ, which is the inverse of the horizontal scale length, is equal to $1.25 \times 10^{-5} m^{-1}$; then,

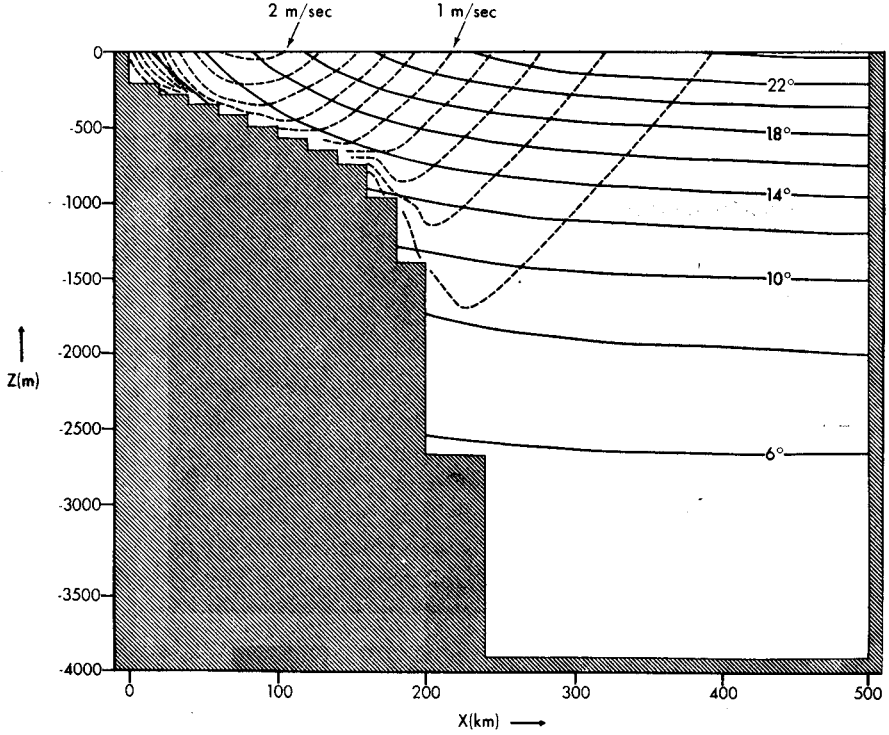

FIGURE 2 A cross section of V and T and the bottom topography in the region considered at the intial time.

ΔT will be approximately 7°C. Also, the vertical variation of the temperature field is given by ε, which is the inverse of the scale height, and is equal to $0.65 \times 10^{-3} m^{-1}$. This profile just described corresponds roughly to the conditions of the Gulf Stream at 35°N latitude.

The Equations (1.2), (1.8), and (1.9) give the relationship between V and T. For a flow which is steady state and in geostrophic balance, the vertical

shear is related to the horizontal temperature gradient (thermal wind relation):

$$V_z = \frac{p_{xz}}{2\Omega\rho_o n_o} = \frac{-g\alpha T_x}{2\Omega n_o}. \tag{2.3}$$

Using the temperature profile definition, Eq. 2.1, and integrating the vertical shear, V_z, we obtain the corresponding velocity profile:

$$V_{(x,z)} = \frac{g\alpha}{2\Omega n_o}\left(\delta^2 x e^{-\delta x}\right)\frac{\Delta T}{\varepsilon}\left(\frac{3}{2} - \varepsilon z\right)e^{2\varepsilon z} \tag{2.4}$$

The cross section of V and T and the bottom topography in the area considered are shown in Figure 2. With the initial conditions discussed, we let the system run for about 100 time steps or until the system is in complete equilibrium [notice that the geostrophic balance does not account for the dissipation terms in Equations (1.2) and (1.3)]. Now, in order to let the system choose the proper scale of motion, we disturb the equilibrium state, at one time only, with a small random perturbation in all fields.

Unfortunately, due to the limitations of the computer, we are able to choose only four different cases; these differences are shown in Table 1. (DX, DY, DT are the cross stream, down stream and time intervals respectively; L is the length of the channel). In all four experiments there were 60 grid points North to South, 25 grid points East to West, and 15 layers in which the first 10 upper layers are 72 m apart and each consecutive layer thereafter has a depth equal to twice the depth of the previous layer. The first experiment has a coarse resolution in the N-S direction, but this was done to determine which horizontal length would be most predominant. Experiments II and III differ only in their value of horizontal eddy viscosity, A_h whereas, experiments III and IV differ only in the β term of the vorticity equation. In the next section we will discuss the field patterns of the solutions for the different cases.

3. Field pattern characteristics

The response to the initial conditions of the numerical model were quite similar, that is to say, at least for the most predominant scale which develops as a result of the instability in the mean conditions. Therefore, we will only describe the solution for one of the experiments (IV). Figure 3 shows the horizontal pattern for temperature and the N-S velocity, both for the first layer (72 m) and for different time integrations (400–1000 time steps). It is obvious that the initial conditions did not have any y variation and after the perturbation is introduced, the system does not show any distortion after 400 time step integrations. We can see that from time step 400 on, the small random scale imposed begins to organize into larger waves until time step

TABLE I

Description of the different parameters for the four experiments

Experiment	*N-S* *L* km	*E-W* *L* km	*DY* km	*DX* km	A_h cm^2/s	A_v cm^2/s	*Dt* min	*f* sec^{-1}	β $s^{-1}m^{-1}$
I	900	500	15	20	10^6	10^2	20	$.835\times10^{-4}$	0
II	450	500	7.5	20	10^5	10^2	10	$.835\times10^{-4}$	0
III	450	500	7.5	20	10^6	10^2	10	$.835\times10^{-4}$	0
IV	450	500	7.5	20	10^6	10^2	10	$.835\times10^{-4}$	10^{-11}

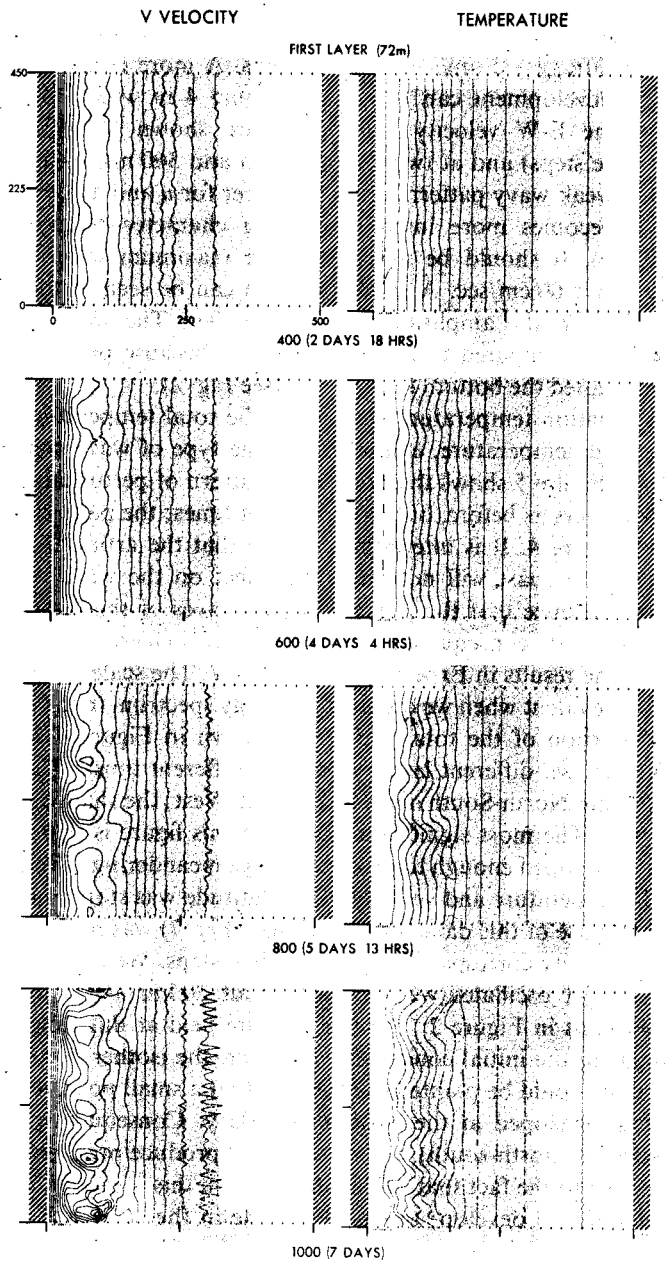

FIGURE 3 Temperature and *N-S* velocity field patterns (Exp. IV) at a depth of 72 m for time steps 400–1000.

1000 where a fully developed wave pattern is clearly seen. The contours of the N-S velocity have the same evolution from random noise to a full wave-like behavior after 1000 time step integrations. A more comprehensive view of the wave development can be seen in Figure 4 in which the horizontal patterns of the E-W velocity component are shown for different times (600–1200 time steps) and at two depths (72 m and 360 m). At time step 600 we can see a weak wavy pattern in the first layer for u and as time progresses the pattern becomes more intense having a characteristic wavelength of $L/4$ (112.5 km). It should be noted that the maximum intensity of the u velocity is about 60 cm/sec. A similar pattern can be seen in the deep layer (360 m); however, the amplitude is much smaller. The short extension of the ellipsoids as compared to the upper layer is because part of layer 5 has already intercepted the bottom topography (see Fig. 2).

The perturbation temperature, defined as the total temperature minus the mean y average temperature, exhibits the same type of wave characteristics. Accordingly, Figure 5 shows the horizontal pattern of perturbation temperature for two layers as before, but with different times; the patterns are similar to those of Figure 4. It is interesting to note that the artificial East wall at 500 km from the coast will not have any effect on the wave development. Also, we can deduce that the β effect on the waves of the order of 100 km scale will have little consequence. This deduction is clearly supported by the similarity of the results in Experiments III and IV. The scale of the waves will become more evident when we discuss the energy spectrum in the next section.

A small portion of the total channel is shown in Figure 6 with velocity vectors for the two different layers and three different times. The size of the region is 150 km North-South and 250 km East-West; the shaded part denotes the West wall. The most significant feature in this figure is that after 8 days the wave is developed enough to produce a large meandering of the jet.

Data for temperature and velocity at one latitude was stored for every time step. With the use of this data, a cross section (Fig. 7) was made for temperature and V velocity corresponding to 1000 time steps. We can notice that the center of the jet oscillates west to east about 20 km as compared to the initial conditions in Figure 2. The temperature field at this time step (1000) looks similar to the initial conditions; however, the isotherms are somewhat more wavy. It should be pointed out though, that a small positive slope of the isotherms is developed at the eastern boundary. Consequently, an eastern counter-current, (north-south), will develop and produce profound dynamical differences due to the fact that horizontal shear in this area will cause a barotropic instability to develop; this is noticeable in the right side of Figure 5. The development of the counterflow can be explained by our artificial eastern wall. Since the total transport is constant across the channel and also because the baroclinic waves in the left side of the channel have the net effect of

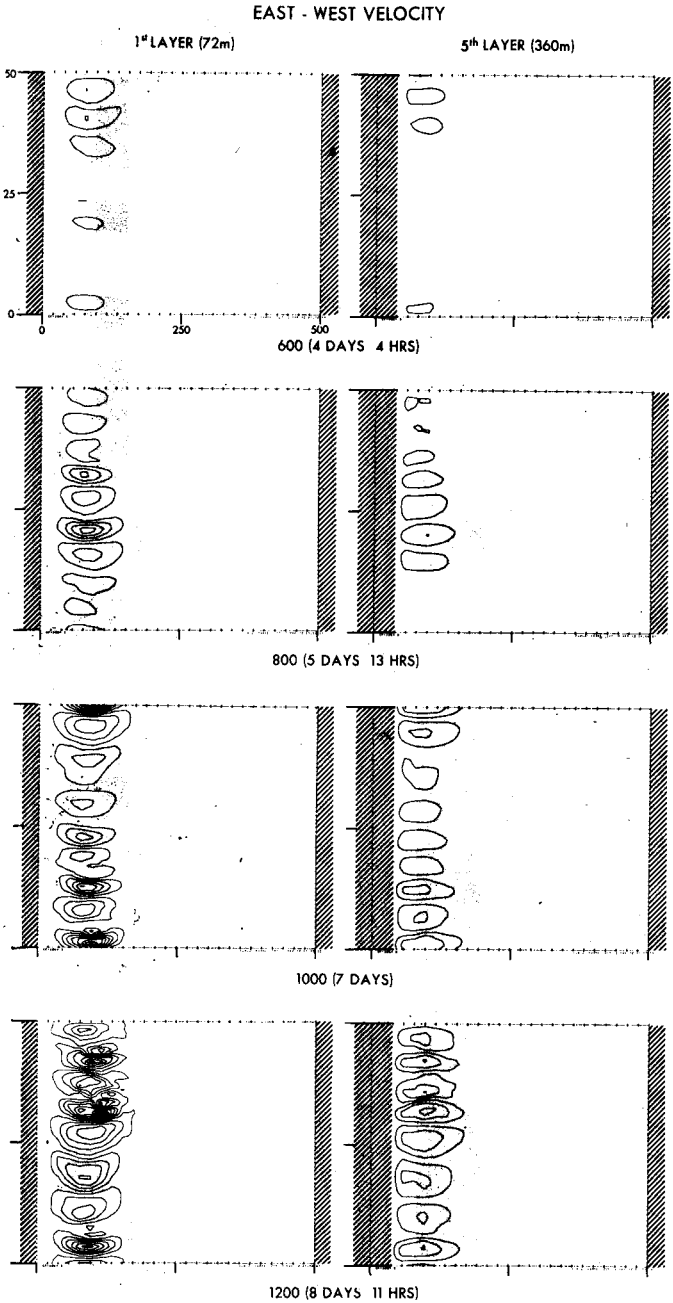

FIGURE 4 The *E-W* velocity patterns as a function of depth (72 m and 360 m) and time integrations (600–1200).

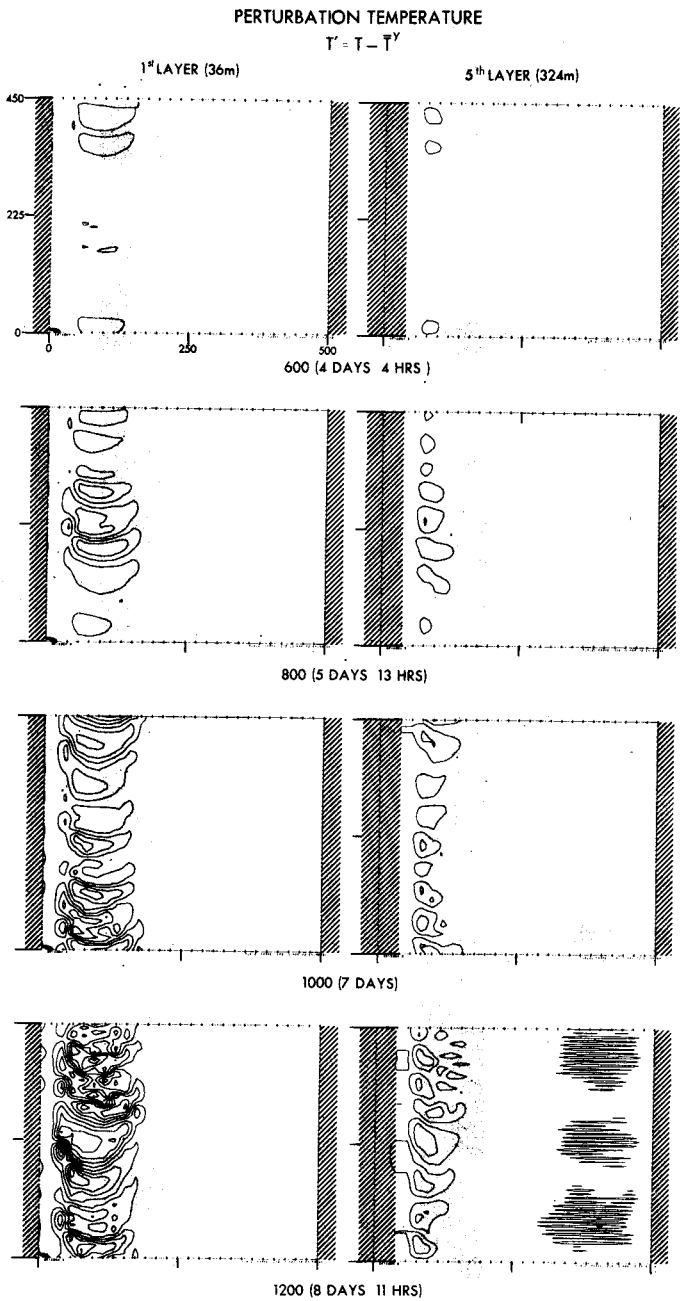

FIGURE 5 The perturbation temperature as a function of depth (36 m and 324 m) and time integrations (600–1200).

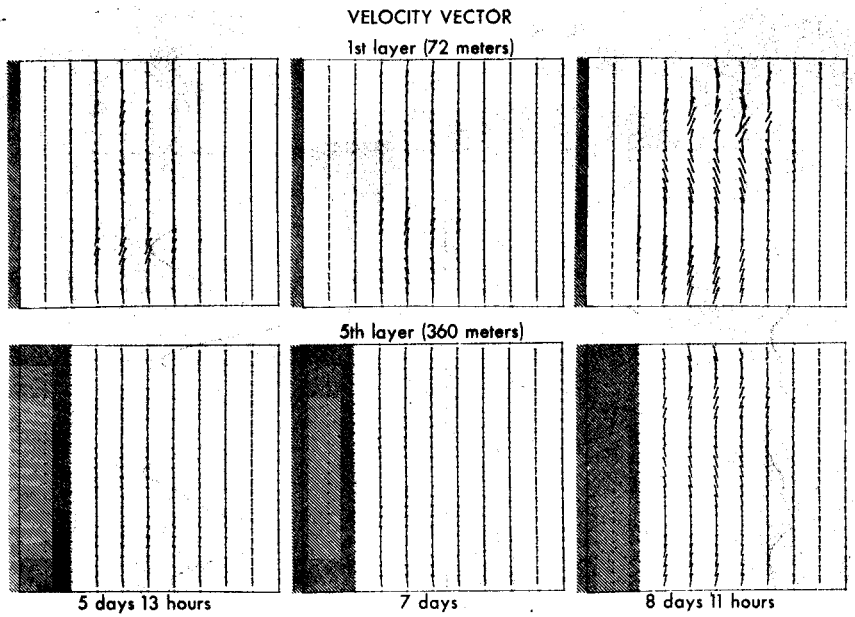

FIGURE 6 The total velocity vector is shown for a portion of the channel at 72 m and 360 m and from about 5.5 to 8.5 days after the initial perturbation.

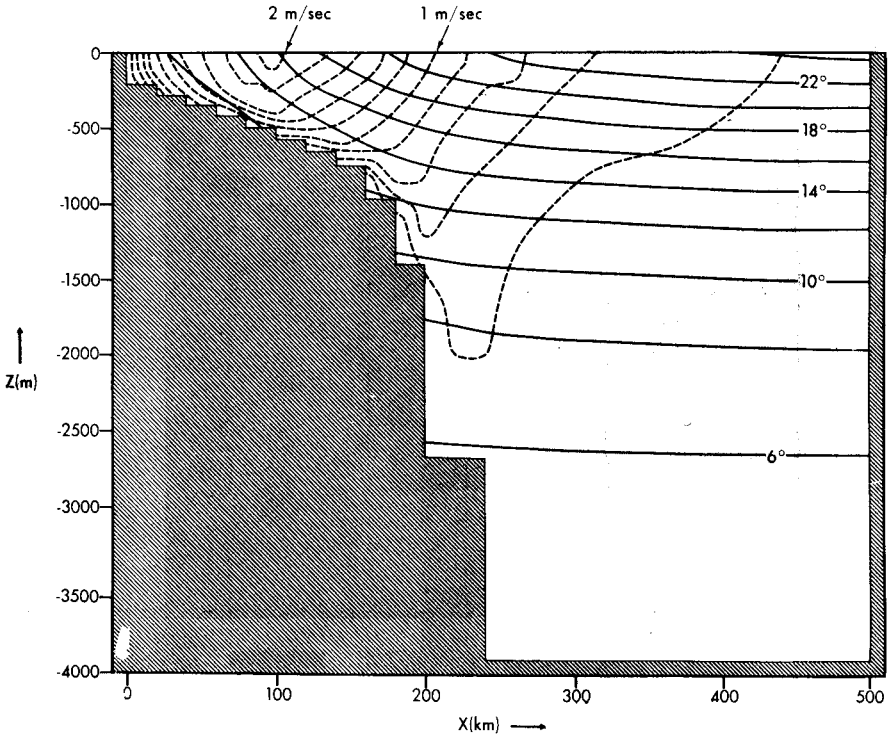

FIGURE 7 A cross section of V and T and the bottom topography in the region considered after 1000 time integrations.

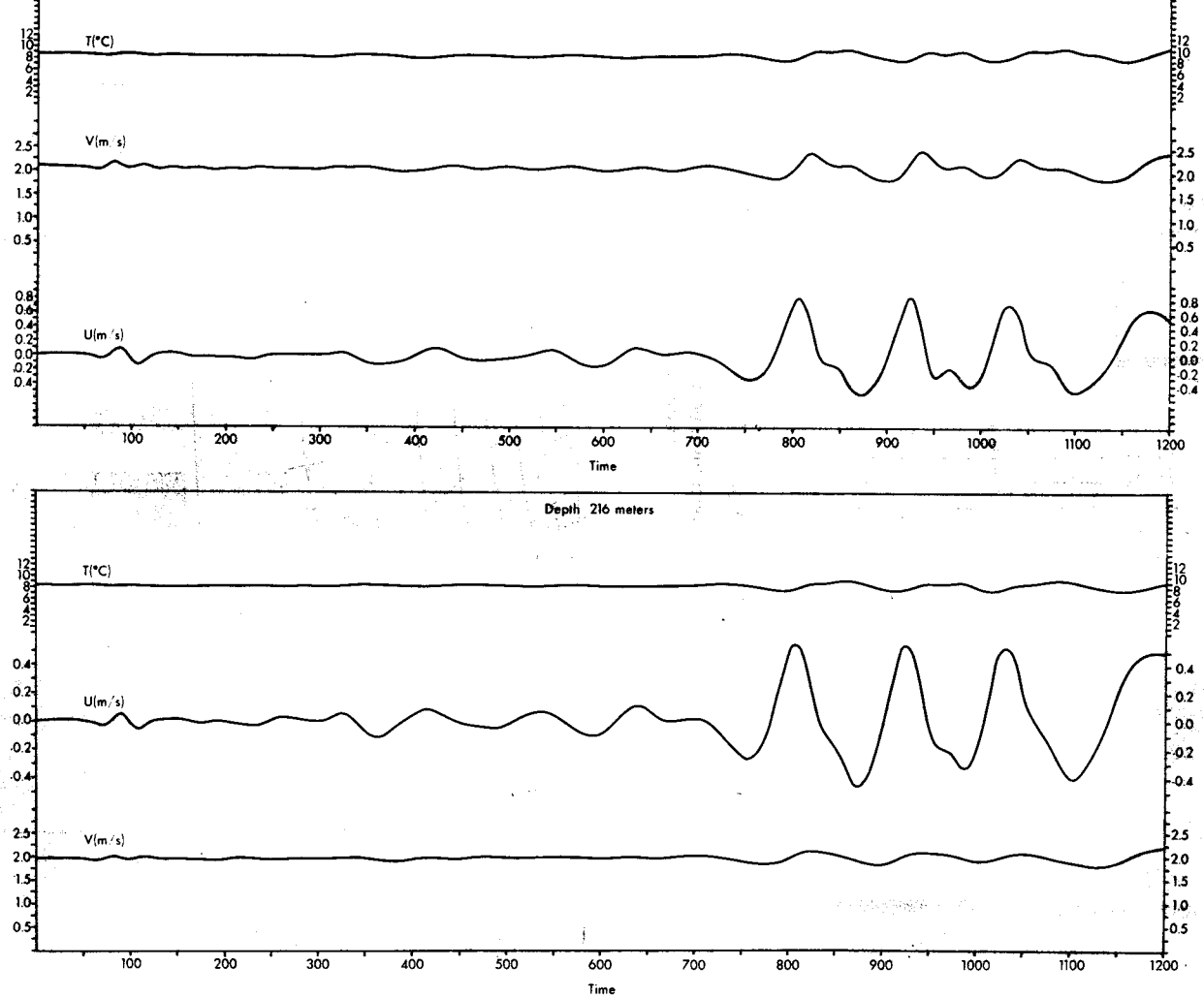

FIGURE 8 The variation of T, U, and V at a fixed point $X = 100$ km in space for 72 m (top) and 216 m (bottom) as a function of time.

increasing the transport there, it is natural to expect that the counter-current will exist, such that the transport will remain constant. This effect is only noticeable after 1000 time integrations. In the energetics section, further information will be given to support this transport effect.

Figure 8 shows the temperature, T and (u,v) velocities, at a fixed point ($x = 100$ km) in space as a function of time. As with the previous figures discussed, the response in these fields is fairly steady for about 500 time steps. Thereafter, a large oscillation is noticeable in all fields. The period of the oscillation is about one day which is close to the natural period. We should like to mention that the waves are a product of baroclinic instability which will be shown later. The remarkable difference between the period for those baroclinic waves and the baroclinic waves of the atmosphere, which have periods of a few days, is the horizontal wavelength of such waves; the atmospheric ones have scales on the order of a thousand kilometers and the oceanic ones are on the order of a hundred kilometers in agreement with our previous scale analysis.

4. Spectral analysis

Due to the periodic boundary conditions at the north-south boundaries, we can Fourier decompose the solutions and follow the physical characteristics of each independent wave. Any of the physical quantities, temperature, velocity, etc., will be decomposed in the following way:

$$\varphi(x,y,z,t) = \sum_N \varphi_N^s \sin\frac{n2\pi}{L}y + \varphi_N^c \cos\frac{n2\pi}{L}y \tag{4.1}$$

where $\varphi_N^s(x,z,t)$ and $\varphi_N^c(x,z,t)$ are defined as follows:

$$\varphi_N(x,t)\Big|_N^s = \frac{1}{\sqrt{2\pi}}\int_0^{2\pi} \varphi(x,y,z,t) \begin{matrix}\sin\frac{n2\pi}{L}y \\ \\ \cos\frac{n2\pi}{L}y\end{matrix} dy \tag{4.2}$$

The data was analyzed every 50 time steps. However, we will only discuss the results at a fixed x of 100 km, ($I = 5$), where the maximum baroclinic zone occurs. The amplitude of the Fourier components, $([(\varphi_N^s)^2 + (\varphi_N^c)^2]^{\frac{1}{2}})$, will grow exponentially in time for those waves which are unstable. Figure 9 shows the amplitude of the faster growing wave for the experiments performed, that is, Experiment I, where $N = 7$ and $\lambda = 128$ km and Experiments II, III, and IV where $N = 4$ and $\lambda = 112.5$ km. It can be seen that the growth

TABLE II

The wave characteristics like wave length, linear and non-linear growth rate, max amplitude, and time to attain max amp. are shown for Exp. I, III, and I V

EXPERIMENT I						EXPERIMENT III						EXPERIMENT IV					
λ_H KM	σ_1 ($\times 10^{-5}$) SEC^{-1}	σ_2 ($\times 10^{-5}$) SEC^{-1}	ΔT °C	TIME DAYS	HRS	λ_H KM	σ_1 ($\times 10^{-5}$) SEC^{-1}	σ_2 ($\times 10^{-5}$) SEC^{-1}	ΔT °C	TIME DAYS	HRS	λ_H KM	σ_1 ($\times 10^{-5}$) SEC^{-1}	σ_2 ($\times 10^{-5}$) SEC^{-1}	ΔT °C	TIME DAYS	HRS
450	.77	0.19	.275	10	0	450	1.11	0.41	.358	8	8	450	0.0	.69	.344	7	19
225	.57	0.17	.156	7	12	225	1.38		.249	8	8	225	1.11	1.11	.675	8	8
180	.73	0.18	.264	8	8	150	1.10	0.37	.357	8	8	150	.74	0.28	.422	8	8
128.5	.96	0.0	.361	10	0	112.5	1.66	0.23	.710	8	8	112.5	1.28	0.26	.303	8	8
112.5	.38	0.16	.231	10	20	90	1.55	0.0	.302	7	7.2	90	1.04	.15	.355	7	19

rate is constant for the first 600 times steps, thus indicating that the instability develops as the linear theory predicts (Orlanski, 1969). However, at longer times, the wave amplitude levels off and the growth rate diminishes. This effect shows the invalidity of some interpretations of the observational analysis dealing with finite amplitude waves (D. Hansen, 1970) in which a growth rate was inferred for those waves and compared to the linear theories.

If we assume the amplitude has an exponential growth rate, let us say:

$$\varphi = \varphi(x,z)e^{\sigma_i t},$$

then from the slope of the curves we can infer how much the value of σ_i will be in the two regions, that is, the linear one (from 200 to 600), $.96 \times 10^{-5}$ sec^{-1} for Experiment I, for II, III, and IV about 1.2×10^{-5} sec^{-1}; for the finite amplitude region, the value is about $.085 \times 10^{-5}$ sec^{-1} and for II, III, and IV about $.22 \times 10^{-5}$sec^{-1}. A more descriptive picture of the growth rates, for wave numbers in the linear and non-linear range, σ_1 and σ_2 respectively, is shown in Table II; the change in amplitude from the initial conditions to the point where the amplitude levels off as well as the elapsed time to reach the maximum amplitude are shown. We can see that all of the wave numbers reach a maximum amplitude in an interval of about 8 days. A comparison will be made with the values obtained by Orlanski (1969) irrespective of the

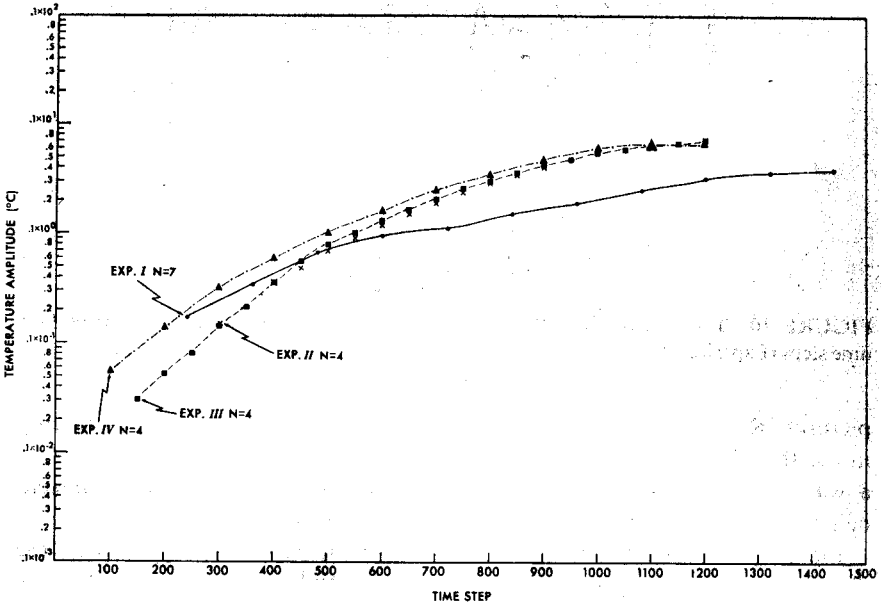

FIGURE 9 The amplitude for the most unstable wave as a function of time is shown for the different experiments.

large difference between the simplified two-layer case and this multi-layer model. The most similar configurations correspond to Figure 17 in the previous paper in which the growth rate of the most unstable wave was estimated to be $\sigma_i = .046$ for a wavelength of 246 km. For similar wavelengths, say for wave number $N = 2$, the estimated initial growth rate corresponds to $\sigma_i = .1$ which is double that predicted by the linear model. Keeping in mind the large difference between the two models, we must conclude that the agreement is reasonably good. Unfortunately, there are no direct oceanic measurements to compare with out solutions; however, a unique set of satellite

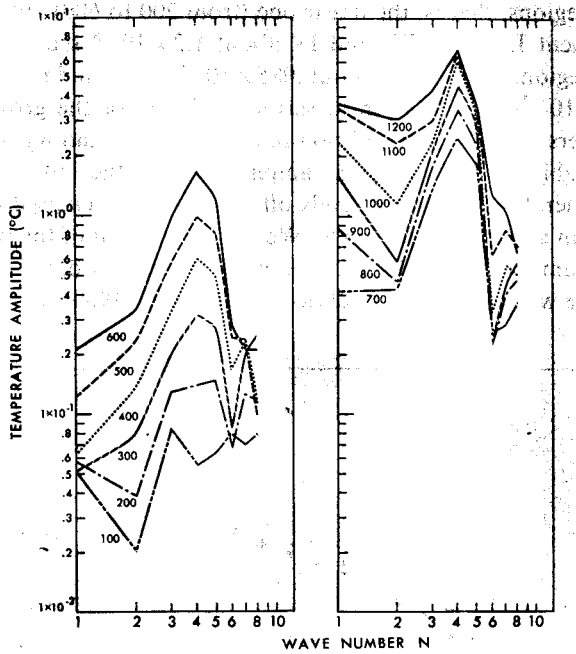

FIGURE 10 The spectral distribution of the temperature amplitude from 100 to 1200 time steps (Experiment IV).

pictures (Rao, 1971) shows that a full wave in the Gulf Stream can develop in less than 15 days. In addition, from the clear wave pattern, we can estimate a wavelength of 120 km. More satellite pictures could reveal the transient behavior of such waves and a better comparison would then be possible.

Figure 10 shows the spectral distribution of the wave amplitude for all the different times in Experiment IV. During the initial times a strong instability is noticeable at wave number 4. From time step 700 on, the mean unstable wave ($N = 4$) decreases its growth rate and reaches a maximum around time

step 1200; also at the former time, another wave (number 1 with a wavelength of 450 km) starts to grow. It is noteworthy to say that, in Experiment I with the channel length doubled, the most unstable waves were $N = 7$ and 2, corresponding roughly to $N = 4$ and 1 in this case (IV). As with wave number 7, wave number 1 reaches a maximum at time step 1200.

In concluding this section, we mention that the phase velocity of the waves (multi-layer model) is close to the mean velocity, 1.5 m/s, corresponding to the layer of strongest baroclinicity. This may appear artificially high but a more realistic profile will give mean velocities on the order of .4 m/s.

5. Energetics of the unstable waves

An important factor in understanding the physics of unstable waves in the coastal boundary jet is the energetics involved in such dynamic processes. Orlanski (1969) discusses the energetics of the analogous two-layer model in great detail. The energetics of the multi-layer model in this case will be analyzed in a similar manner.

Suppose that we define a mean quantity as follows:

$$\Phi(x,z,t) = \frac{1}{L}\int_{y0}^{y0+L} \phi(x,y,z,t)\, dy \tag{5.1}$$

then the fluctuation quantities are:

$$\phi'(x,y,z,t) = \phi(x,y,z,t) - \Phi(x,z,t) \tag{5.2}$$

The same averaging procedure can be applied to the equations of motion (1.2–1.10) and then substituting them into the original system (1.2–1.10) will result in a new system for fluctuation quantities defined as follows:

$$u'_t + (\mathscr{L}u)' - 2\Omega\mu_o v' = -\left(\frac{p}{\rho_o}\right)'_x + F'^x \tag{5.3}$$

$$v'_t + (\mathscr{L}v)' - 2\Omega\mu_o v' = -\left(\frac{p}{\rho_o}\right)'_y + F'^y \tag{5.4}$$

$$T'_t + (\mathscr{L}T)' = \frac{A_v}{\delta} T'_{zz} + A_h (T_{xx} + T_{yy})' \tag{5.5}$$

$$\nabla . \mathbb{V}' = 0 \tag{5.6}$$

$$-p'_z = g\rho' \tag{5.7}$$

This system is such that the y average will be identically zero. The fluctuation advective terms are:

$$(\mathscr{L}\mu)' = \mathbb{V}' . \nabla\bar{\mu} + \bar{\mathbb{V}} . \mu' + \mathbb{V} . \nabla\mu' - \overline{\mathbb{V}' . \nabla\mu'} \tag{5.8}$$

It is easy to verify that:

$$(\mathscr{L}\mu) = \overline{(\mathscr{L}\mu)} + (\mathscr{L}\mu)' \tag{5.9}$$

where

$$(\mathscr{L}\mu) = \bar{\mathbb{V}} \cdot \nabla\bar{\mu} + \overline{\mathbb{V}' \cdot \nabla\mu'} .$$

The average of the advection terms is equal to the advection of mean quantities plus the integrated effect of the advection of the fluctuation quantities.

The total horizontal kinetic energy is given by the volume integral of the density energy:

$$K_T = \iiint \rho_o \left(\frac{u^2+v^2}{2}\right) dz\, dy\, dx \tag{5.10}$$

Since $u = \bar{u}+u'$ and $v = \bar{v}+v'$, K_T can be expressed as:

$$K_T = \iiint \frac{\bar{u}^2+\bar{v}^2}{2} \rho_o\, dv + \iiint \frac{u'^2+v'^2}{2} \rho_o\, dv = K_m + K_e , \tag{5.11}$$

where K_m is the mean kinetic energy and K_e is the eddy kinetic energy. With the help of the system (5.3–5.7) we can derive the time variation of the eddy kinetic energy by adding equations (5.3) multiplied by u' to (5.4) multiplied by v' and integrating over the total volume.

$$L\iint\left(\frac{\bar{u}'^2}{2}+\frac{\bar{v}'^2}{2}\right)_t dz\, dx + L\iint[\overline{(\mathscr{L}u)'u'} + \overline{(\mathscr{L}v)'v'}]$$

$$= -L[\iint(\overline{p_x'u'} + \overline{p'_y v'})\, dx\, dz + \iint \overline{F'^x}u' + \overline{F'^y}v'\, dx\, dz] \tag{5.12}$$

Since the first term on the left represents the time variation of the eddy kinetic energy, the other three integrals represent sources or sinks of eddy kinetic energy. The second integral on the left in (5.12) can be expressed as follows by using (5.8):

$$(\mathscr{L}u)'u' + (\mathscr{L}v)'v' = \overline{u'\mathbb{V}'} \cdot \nabla\bar{u} + \bar{\mathbb{V}} \cdot \nabla\frac{\bar{u}'^2}{2} + \overline{\mathbb{V}' \cdot \nabla\frac{u'^2}{2}}$$

$$+\overline{v'\mathbb{V}'} \cdot \nabla\bar{v} + \bar{\mathbb{V}} \cdot \nabla\frac{\bar{v}'^2}{2} + \mathbb{V}' \cdot \nabla\frac{\bar{v}'^2}{2} = \tag{5.13}$$

$$\overline{u'\mathbb{V}'} \cdot \nabla\bar{u} + \overline{v'\mathbb{V}'} \cdot \nabla\bar{v} + \mathbb{V} \cdot \nabla\frac{u'^2+v'^2}{2}$$

Notice that the average of the last term in (5.8) is multiplied by a fluctuation quantity and is zero; therefore, is it not included in (5.13). The last term in (5.13) is the advection of eddy kinetic energy by the total flow and the other two terms are the conversion of energy between the mean and eddy kinetic energy by Reynolds stresses. Then, the volume integral of the terms in (5.13),

remembering that the periodic and rigid boundaries produce zero net flux of kinetic energy, is

$$\iint \overline{\nabla \cdot \left(\frac{u'^2+v'^2}{2}\right)} \, dz \, dx = 0 .$$

Then the remaining terms are:

$$L\iint[\overline{(\mathscr{L}u)'u'}+\overline{(\mathscr{L}v)'v'}] \, dz \, dx = L\iint[\overline{u'v'}\bar{U}_x+\overline{u'w'}\bar{U}_z + \overline{v'u'}\bar{V}_x+\overline{v'w'}\bar{V}_z] \, dz \, dx \tag{5.14}$$

Since the initial mean flow is characterized by a velocity $\bar{V}(x,z)$ and the fluctuation vertical velocity is far smaller than the horizontal velocity, it is convenient to split (5.14) into two terms:

$$\iint[(\mathscr{L}u)'u'+(\mathscr{L}v)'v'] = -\int I_1 \, dx - \int I_2 \, dx \tag{5.15}$$

where $I_1 = -\int_{h(x)}^{0} \overline{u'v'}\bar{V}_x \, dz$

and $I_2 = -\int_{h(x)}^{0} [u'^2\bar{U}_x+\overline{v'w'}U_z+v'w'\bar{V}_z] \, dz$

The next terms that we will expand are the integrals containing the pressure terms in (5.12),

$$\overline{u'p'_x}+\overline{v'p'_y} = (\overline{p'u'})_x+(\overline{p'v'})_y+(\overline{p'w'})_z+g\overline{\rho'w'} \tag{5.16}$$

and since the total effect of work done by pressure forces at the surface of the domain is zero, the volume integral of (5.16) is:

$$L\iint u'p'_x+v'p'_y \, dz \, dx = L\iint g\overline{\rho'w'} \, dz \, dx = -L\iint \rho_o g\alpha\overline{T'w'} \, dz \, dx \tag{5.17}$$

The dissipation of energy due to viscous forces are:

$$\overline{u'F'^x}+\overline{v'F'^y} = A_h\overline{u'\nabla^2u'}+A_v\overline{u'u'_{zz}}+A_h\overline{v'\nabla^2v'}+A_v\overline{v'v'_{zz}} \tag{5.18}$$

Finally, we can express the time change of eddy kinetic energy (5.12) as follows:

$$\int_0^L\int_H^0 K_{et} \, dz \, dx = \int(I_1+I_2) \, dx + \int_0^L\int_H^0 \rho_o g\alpha\overline{T'w'} \, dz \, dx + \iint(A_h\overline{\mathbb{V}'\cdot\nabla^2\mathbb{V}'}+A_v\overline{\mathbb{V}'\cdot\mathbb{V}'_{zz}}) \, dz \, dx \tag{5.19}$$

The interpretation is simple. The time rate of change of eddy kinetic energy is given by a conversion of mean kinetic to eddy kinetic energy by Reynolds

stresses:

$$\langle K_m, K_e \rangle = \int (I_1 + I_2)\, dx\,,$$

a conversion of potential to eddy kinetic energy:

$$\langle P_e, K_e \rangle = \iint \rho_o \alpha T' w'\, dz\, dx = I_3\,,$$

and the loss of energy by dissipation:

$$\text{Diss} = \iint (\mathbb{V}' \cdot \nabla^2 \mathbb{V}' + \ldots)\,.$$

A similar balance equation can be derived for the temperature squared which is related to the potential energy contained in the fluctuation field. If we multiply (5.5) by T' and integrate over the whole volume, we have:

$$\iint \left(\frac{\bar{T}'^2}{2}\right)_t dz\, dx = -\left[\iint \overline{T'\mathbb{V}'} \cdot \nabla_h \bar{T}\, dz\, dx + \iint T' w' \bar{T}_z\, dz\, dx \right.$$

$$\left. + \iint \frac{A_h}{\delta} \overline{T' \nabla^2 T'} + \iint A_v T' T'_{zz}\, dz\, dx \right] \tag{5.20}$$

Moreover, if we compare Figs. 2 and 7, we notice that the mean temperature does not change much with the evolution of the waves. Therefore, we are justified in multiplying (5.5) by $-g\alpha(T'/\bar{T}_z)$ and integrating over the total volume; thus we obtain a balance equation for the eddy potential energy:

$$\iint P_{et}\, dz\, dx \quad \iint \frac{g\alpha}{\bar{T}_z} \overline{T'V'} \nabla_h \bar{T}\, dz\, dx - \iint g\alpha \overline{T'w'}\, dz\, dx$$

$$+ \text{Diss. of Pot. Energy}\,, \tag{5.21}$$

where the left term is the time rate of change of eddy potential energy which is balanced by the conversion of mean potential to eddy potential energy:

$$\langle P_m, P_e \rangle = \iint \frac{g\alpha}{\bar{T}_z} \overline{T'V'}\, dz\, dx\,,$$

minus the conversion of eddy potential to eddy kinetic energy $\langle P_e, K_e \rangle$, plus the dissipation of eddy potential energy. Notice that even though (5.20) appears to be exactly the same as (5.21), they are not the same because the mean temperature is not only a function of z, but also a function of x and t as well. If we remove this assumption, there will be extra terms in (5.21) that will be added to the conversion of mean potential to eddy potential energy; however, those terms are very small and independent computation of the four integrals in (5.21) shows a very good balance.

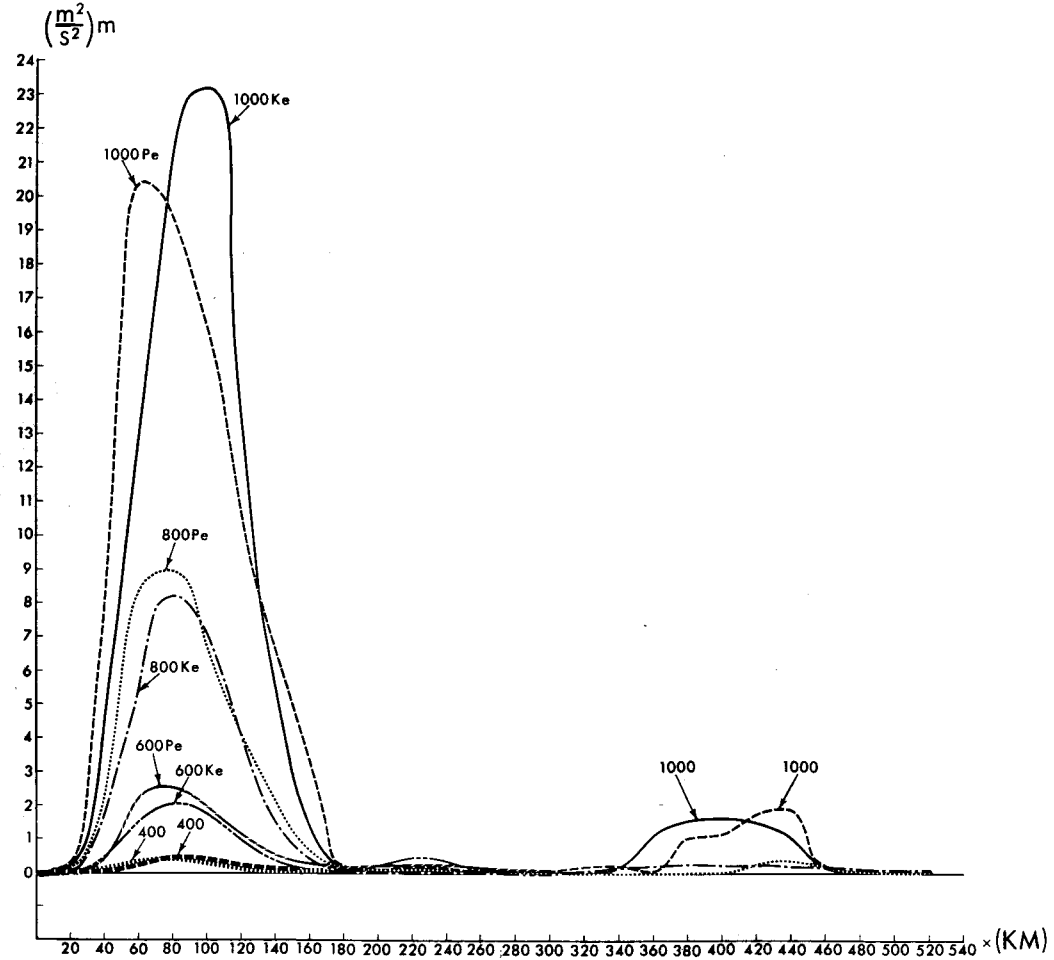

FIGURE 11 Eddy potential energy and horizontal kinetic energy are shown as a function of the cross stream variable X for 400, 600, 800, and 1000 time steps.

The eddy potential energy equal to:

$$\iint -g\alpha \frac{\bar{T}'^2}{\bar{T}_z}\, dy\, dz$$

as previously defined in (5.21) and the horizontal kinetic energy equal to:

$$\iint \rho_o \left(\frac{u'^2}{2} + \frac{v'^2}{2} \right) dy\, dz$$

as previously defined in (5.11) are shown in Figure 11 as a function of the cross stream variable, x, for different times; accordingly, at these times, we can observe the exponential growth from the maximum peak. All of the eddy energy is mostly concentrated in the zone of maximum baroclinicity; however, it is possible to notice that the amount of energy close to the east boundary is not zero and this energy is mostly contained in the internal inertial gravity waves which have scales smaller than the mean unstable wave. There is a flux of energy from the baroclinic zone to the wall that excites these gravity waves and even if the amount of energy is small compared with that of the mean wave, the time rate of change of energy can be large.

In Figure 12 all of the terms of the mean square temperature ($\bar{T}'^2$) are shown for time step 400. There is a complete balance between the time variation of the mean square temperature and $-\overline{T'w'}\bar{T}_z$ on the right side of the channel. On the left side, however, the time rate of change of mean square temperature plus $-\overline{T'w'}\bar{T}_z$ is equal to $-\overline{T'u'}\bar{T}_x$. After 400 time steps, Figure 13 shows the same behavior. The primary difference is that the amplitude is larger in the latter. It should also be noted that the mean square temperature is related to the eddy potential energy; $-\overline{T'u'}\bar{T}_x$ is related to the transfer of mean potential energy to eddy potential energy and $-\overline{T'w'}\bar{T}_z$ is related to the conversion of eddy potential energy to eddy kinetic energy (see the definition of I_3). Keeping these things in mind, we can see that the mean potential energy provides the source in the left side of the channel where the baroclinicity is strong, thus causing the system to become baroclinically unstable and a small amount of energy flux to be induced to the right side of the channel producing an internal gravity wave oscillation with a relatively high frequency as compared to the baroclinic waves of the left side. This explains why the time variation of the squared temperature is larger on the right side of the channel (the period of those internal gravity waves is about 2 hours and the wavelengths are on the order of 40 km).

In Figures 14 and 15 all the terms which enter into the kinetic energy equations are shown, that is, K_{e_t} which is the time rate of change of eddy kinetic energy, I_1, I_2, I_3, etc. A clear balance can be seen between the time rate of change of kinetic and $I_3 = g\alpha \int \overline{T'w'}\, dz$ which is the term responsible to

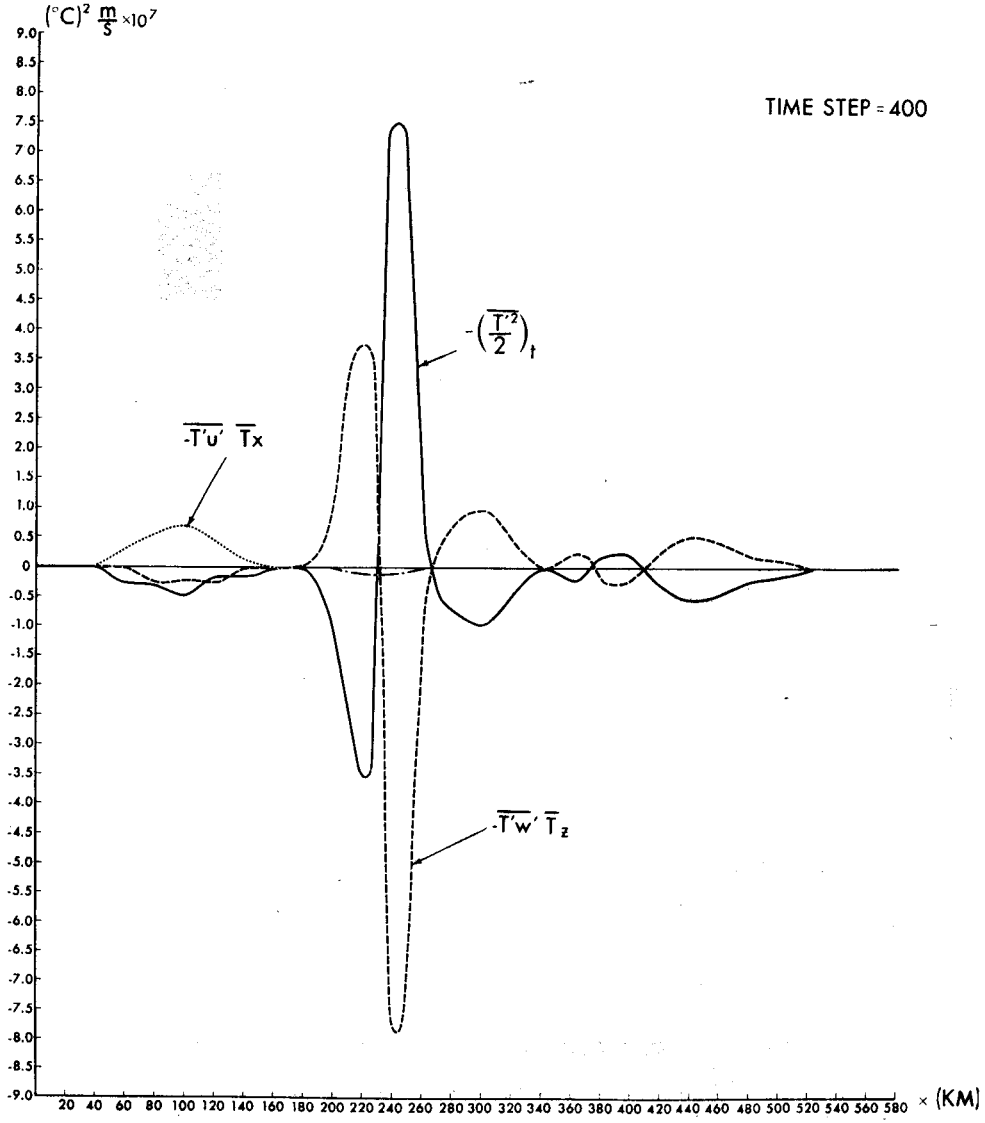

FIGURE 12 The terms for the mean square temperature at time step 400 are shown (see text).

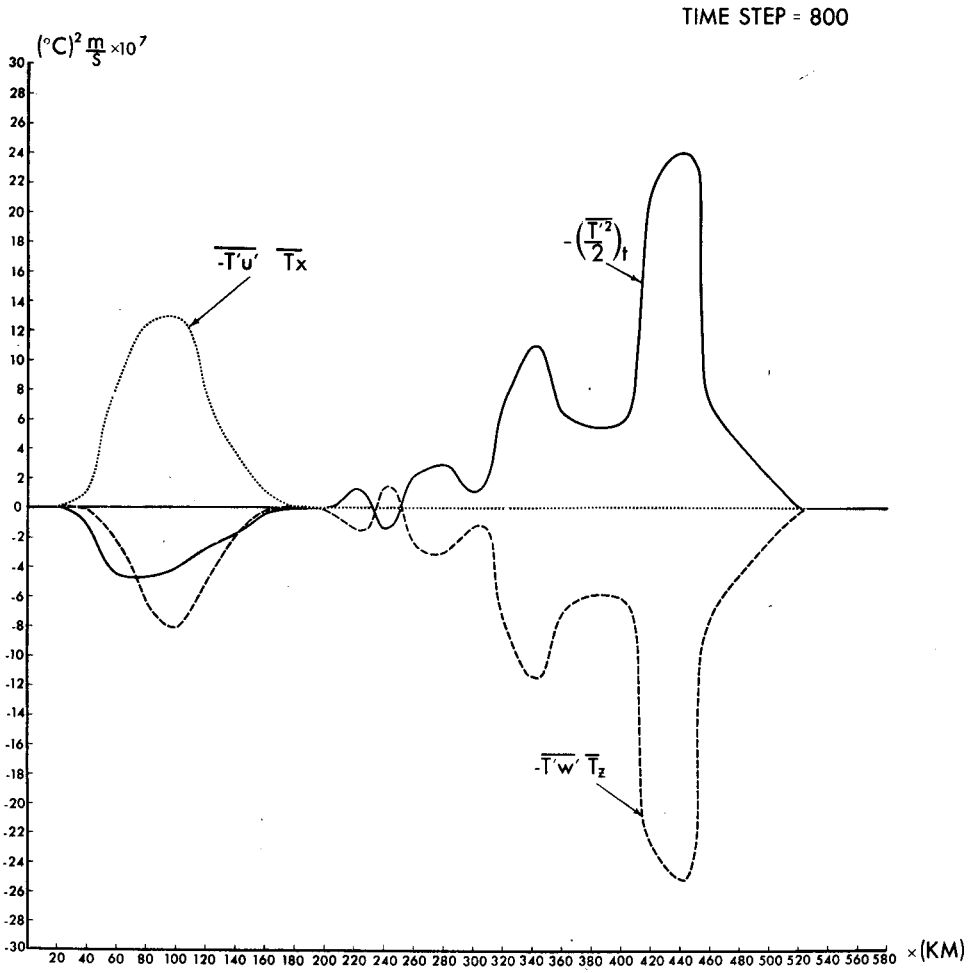

FIGURE 13 The same as Figure 12 with time integration 800.

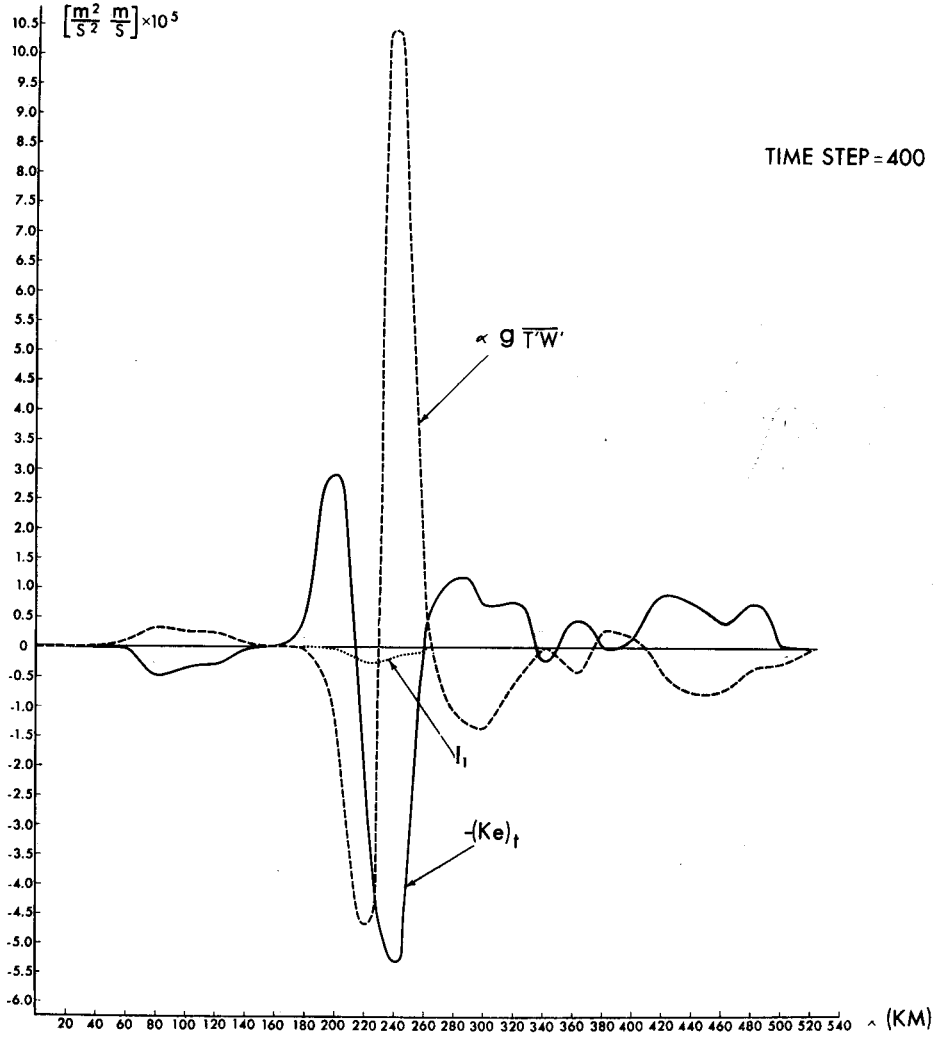

FIGURE 14 Terms which enter into the kinetic energy equations. The curves are drawn for time step 400 (see text).

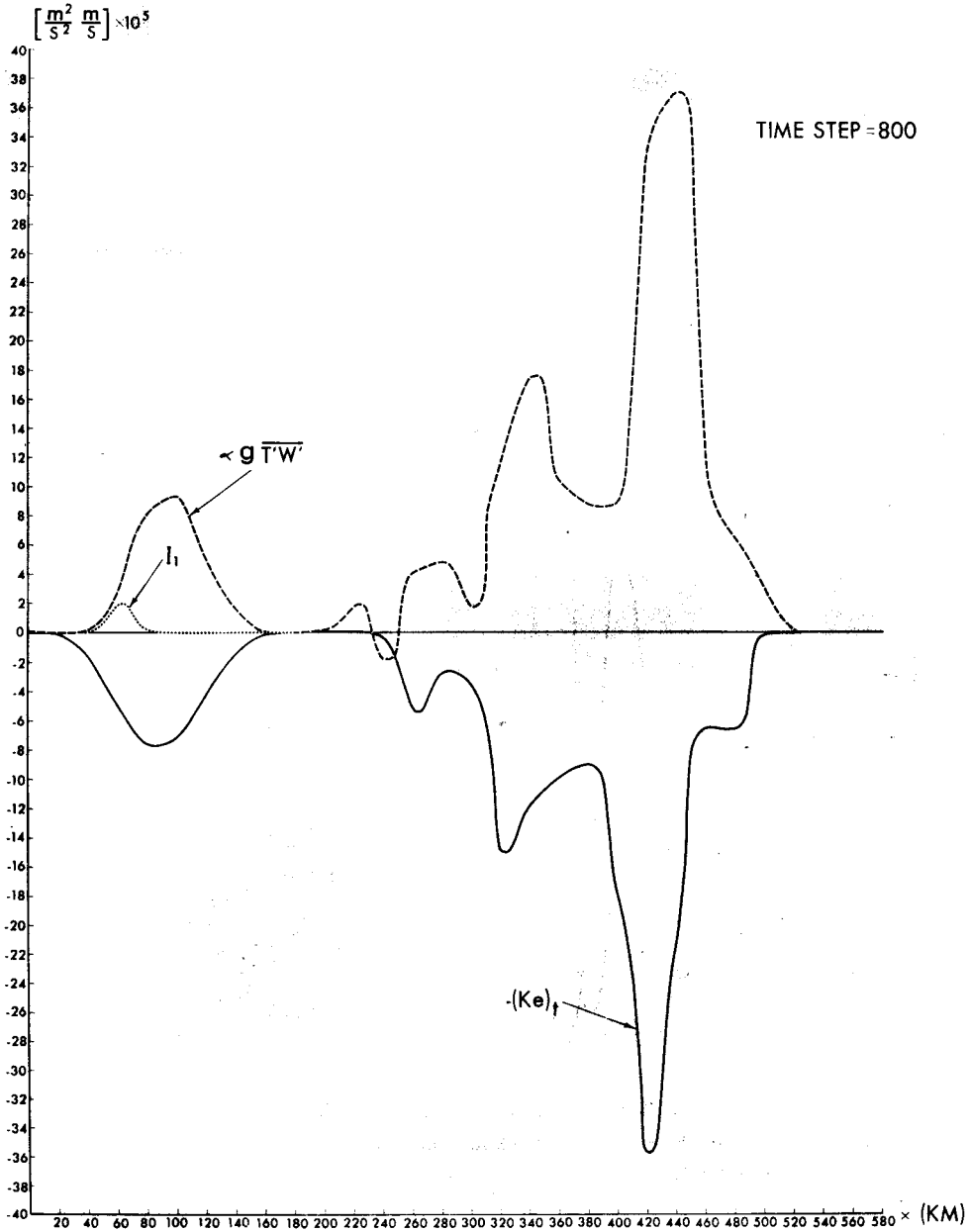

FIGURE 15 The same as Figure 14 with time integration 800.

convert eddy potential energy to eddy kinetic energy. The total integral of this term shows that there is a net transfer from eddy potential energy to eddy kinetic energy, a characteristic result of a baroclinically unstable wave. Comparitively speaking, these waves, as with baroclinic waves in the atmos-

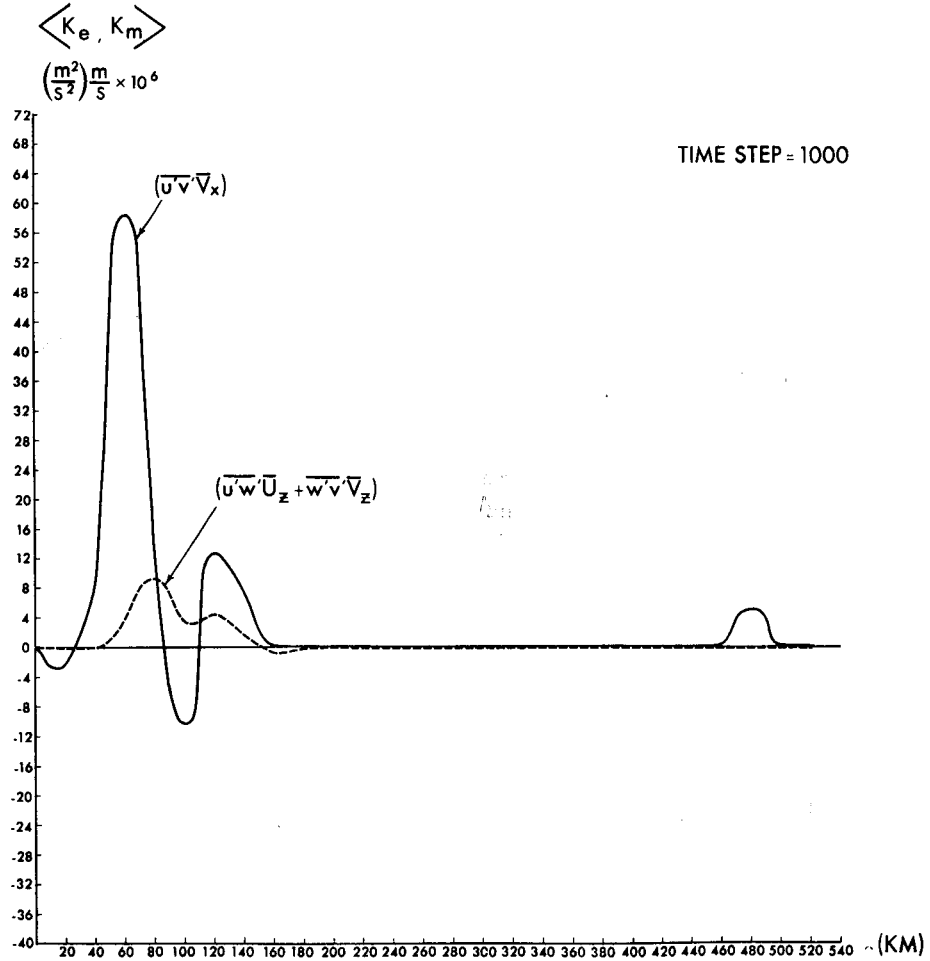

FIGURE 16 The conversion of eddy kinetic energy to mean kinetic energy due to the Reynolds stress, after 1000 time steps.

phere, can be seen to drain energy from the mean potential energy and as the eddy energy of the waves is increasing, a small amount of energy is lost by feedback to the mean flow due to horizontal Reynolds stresses. Accordingly, Figure 16 shows the conversion of eddy kinetic energy to mean kinetic energy

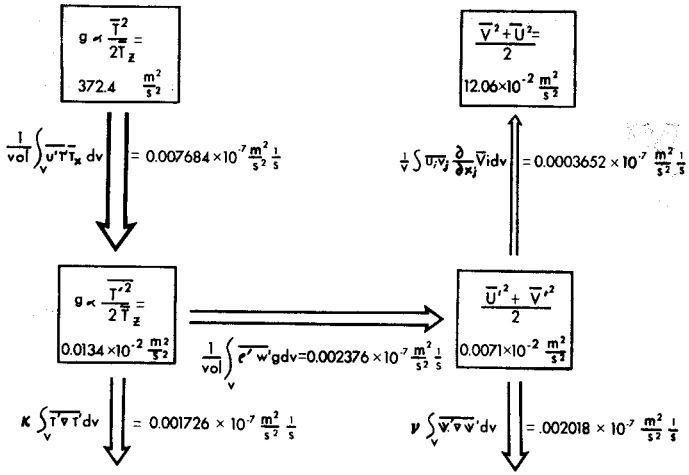

FIGURE 17 The diagram shows the volume integrals and balance of energy after 400 time integrations.

due to the Reynolds stresses. A strong analogy can be seen between the curve obtained by Webster (1961), for the energetics of the Gulf Stream which were calculated from observed data, and the results of the two-layer model of Orlanski (1969). The fact that eddies can lose energy to the mean flow (the so-called negative viscosity) has been discussed by Starr (1968).

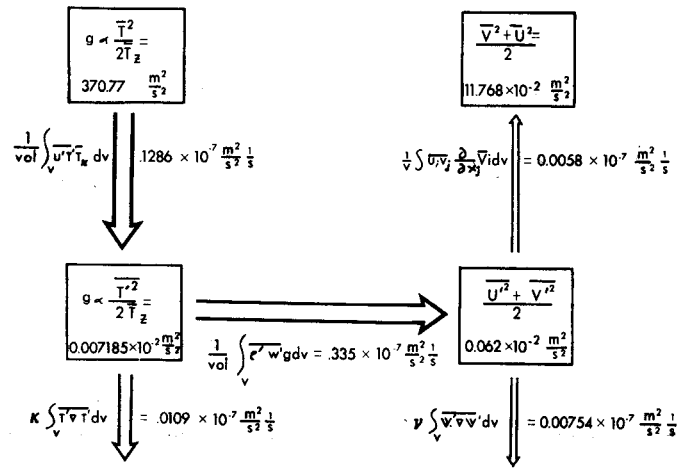

FIGURE 18 The diagram shows the volume integrals and balance of energy after 800 time steps.

We will now show the average volume integrals for the right side of equations (5.19) and (5.21) and also the amount of energy contained in the mean and eddy terms. Figure 17 corresponds to the balance of energy for 400 time step integrations and Figure 18 for 800 time step integrations. It is obvious from these figures that the mean potential energy is the internal source which provides energy to the eddies. This type of dynamic system is well known for long wave atmospheric motion [Charney (1947 and others]. Since the source of these unstable waves is due to the baroclinicity of the flow, it is justified to call them baroclinic waves. As we mentioned before, the atmospheric waves have scales one order of magnitude greater than those of the ocean. An explanation of the difference in scales is that the radius of deformation is about one order of magnitude larger in the atmosphere than in the ocean. Notice that the wavelengths for the unstable waves here are on the order of the radius of deformation and thus is in good agreement with the atmospheric case. Moreover, we can say that baroclinic waves developing in deep sea will have wavelengths of about 400 km; this has already been predicted by Orlanski (1969) in which he compared the unstable waves for jets flowing off the continental shelf and those in the middle of the ocean.

Another characteristic, previously mentioned, is that on the average the waves are losing energy to the mean kinetic energy. Even if the amount of energy is small, it could be enough to counteract the dissipation effects due to viscosity.

In concluding this section, we will briefly discuss the role of baroclinic unstable waves in the so-called eddy viscosity and eddy diffusivity that is used in large scale numerical models. Obviously, numerical models with a grid size of 100 km that cannot resolve wavelengths less than a few hundred kilometers also will not include the baroclinic waves that could be generated in most of the ocean currents. Therefore, in order to simulate the loss or gain in the mean flow that is predicted due to those eddies, the effect is usually parameterized assuming some type of eddy viscosity and eddy diffusivity. The former is defined as the Reynolds stresses divided by the mean shear flow and the latter is the correlation between the temperature and velocity fluctuations divided by the mean temperature gradient. We can then define the eddy viscosity and eddy diffusivity as follows:

$$\nu_H = -\overline{\left(\frac{\overline{u'v'}^{y}}{\bar{V}_x^{y}}\right)}^{z}, \qquad \kappa_H = -\overline{\left(\frac{\overline{T'u'}^{y}}{\bar{T}_x^{y}}\right)}^{z} \tag{5.22}$$

Since we have a way to compute the correlation between the temperature and velocity fluctuations for the baroclinic waves, it would be interesting to show how much those values will be. Accordingly, Figure 19 shows the eddy viscosity as a function of the cross stream variable for different times (400,

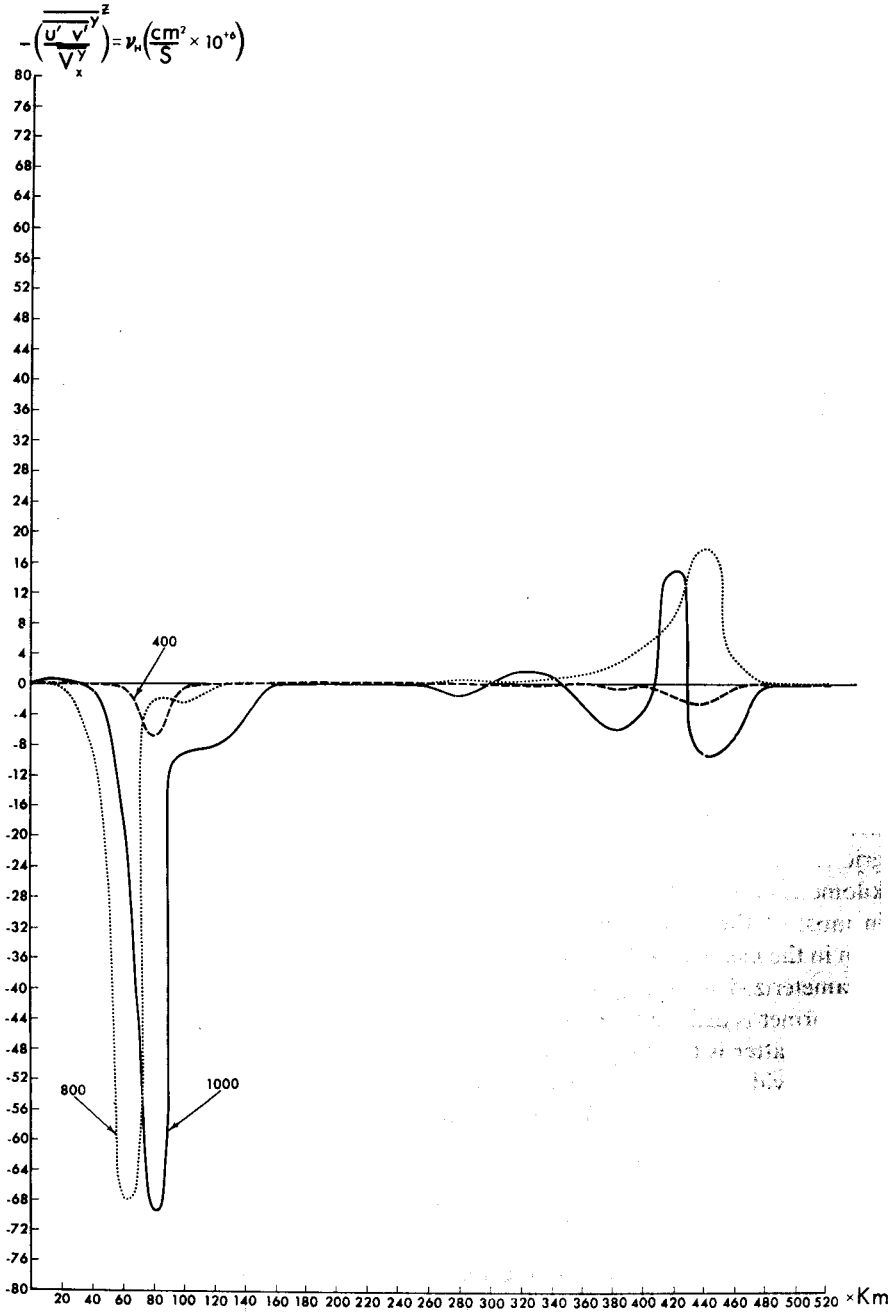

FIGURE 19 Eddy viscosity is shown as a function of the cross stream variable for 400, 800, and 1000 time integrations.

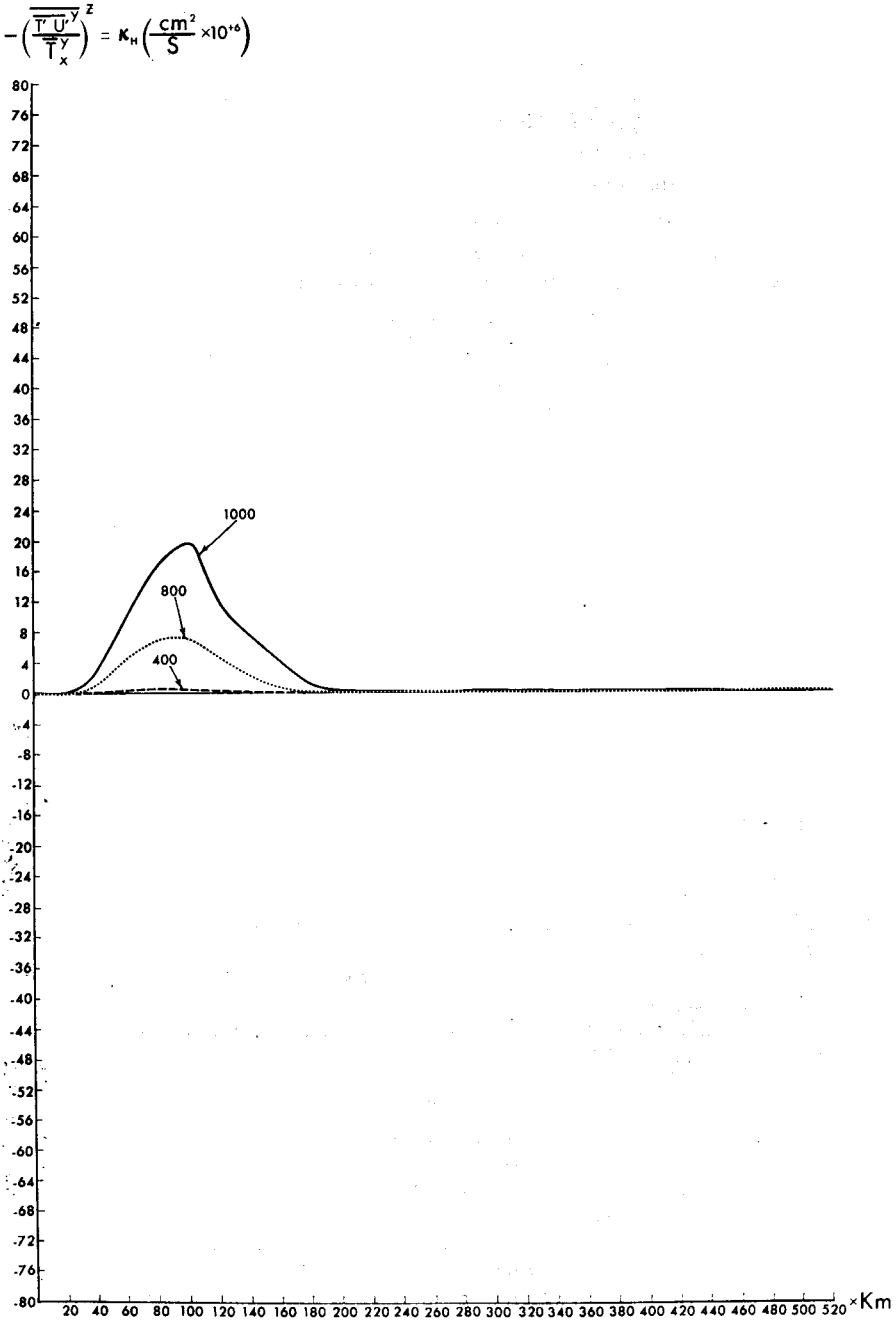

FIGURE 20 Eddy diffusivity is shown as a function of the cross stream variable for 400, 800, and 1000 time integrations.

800, 1000). It is possible to see that a very strong negative eddy viscosity is in the region of a jet, thus implying that the jet itself gains momentum from the eddies as we have already shown in Figures 17 and 18. Far from the zone of maximum baroclinicity on the right side of the channel, an opposite effect can be noticed in that the net effect of eddy viscosity is positive. This is caused by a small scale barotropic instability which may have been artificially excited by the model. The Reynolds stresses in this area are very small, but since eddy viscosity is defined as the Reynolds stresses divided by the mean shear (5.22) and the mean shear is practically zero due to a very small mean flow, it may very well be that the eddy viscosity in this area is not meaningful.

In a similar manner, a positive eddy diffusivity is shown in Figure 20. In being consistent with our previous arguments, a strong loss of heat can be expected in the zone of maximum baroclinicity as the figure indicates.

Acknowledgements

The authors are very grateful and wish to thank A. Hirschman for writing the analysis program used in the energy balance, and L. Polinsky for his analyses of the unstable modes, assistance with the numerical program, and suggestions which helped clarify the paper.

We also wish to extend thanks and appreciation to Dr. K. Bryan, who developed the numerical model and loaned it to the authors for this study. Our thanks also to M. Jackson, P. Tunison and Y. Towns for their assistance in preparing the manuscript.

References

Bryan, K., "A numerical method for the study of ocean circulation," *J. Computat. Phys.*, **4**, pp. 347–376. (1969).

Bryan, K. and M. D. Cox, "A numerical investigation of the ocean general circulation," *Tellus*, **19**, pp. 54–80. (1967).

Charney, J. G., "The dynamics of long waves in a baroclinic westerly current," *J. Meteor.*, **4**, pp. 135–162. (1947).

Hansen, D., "Gulf Stream meanders between Cape Hatteras and the Grand Banks, *Deep Sea Res.*, **17**, pp. 495–511. (1970).

Orlanski, I., "The influence of bottom topography on the stability of jets in a baroclinic fluid," *J. Atmos. Sci.*, **26**, pp. 1216–1232. (1969).

Pedlosky, J., "The stability of currents in the atmosphere and in the ocean. Part I," *J. Atmos. Sci.*, **21**, pp. 201–219. (1964).

Rao, P. Krishna, A. E. Strong, and R. Koffler, "Gulf Stream meanders and eddies as seen in satellite infrared imagery," *J. Phys. Ocean.*, **1**, pp. 237–239. (1971).

Smagorinsky, J., "General circulation experiments with the primitive equations," *Mon. Wea. Rev.*, **91, 3**, pp. 99–164. (1963).

Starr, V. P., "Physics of Negative Viscosity Phenomena," McGraw-Hill, New York, 256 pp. (1968).

Webster, F., "The effect of meanders on the kinetic energy balance of the Gulf Stream," *Tellus*, **13**, 392–401. (1961).